A Comparative Study of Composition and Morphology Effect of $Ni_xCo_{1-x}(OH)_2$ on Oxygen Evolution/Reduction Reaction

Lei Wang,[†,§,¶] Chong Lin,[†,∇,¶] Dekang Huang,[‡] Fengxing Zhang,[§] Mingkui Wang,[‡] and Jian Jin*,[†]

[†]Nano-Bionics Division and i-LAB, Suzhou Institute of Nano-Tech & Nano-Bionics, Chinese Academy of Sciences, Suzhou, Jiangsu 215123, China

[‡]Wuhan National Laboratory for Optoelectronics, Huazhong University of Science and Technology, Wuhan, Hubei 430074, China

[§]Key Laboratory of Synthesis and Natural Functional Molecular Chemistry (Ministry of Education), College of Chemistry & Materials Science, Northwest University, Xi'an, Shaanxi 710069, China

[∇]University of Chinese Academy of Sciences, Beijing, 100049, China

S *Supporting Information*

ABSTRACT: Oxygen electrochemistry has been intensely studied in the pursuit of sustainable and efficient energy conversion and storage solutions. Over the years, developing oxygen electrode catalysts with high activity and low cost remains a great challenge, despite tremendous efforts. Here, $Ni_xCo_{1-x}(OH)_2$ is used as a bifunctional electrocatalyst for both oxygen evolution reaction (OER) and oxygen reduction reaction (ORR). The effect of its compositions ($x = 1, 0.55, 0$) and morphologies (including both multilayer and single-layer $Ni_xCo_{1-x}(OH)_2$) on catalytic activity is studied systematically in order to optimize the oxygen-electrochemical performance of 3d-M (M = Ni and Co) metal hydroxides. Our results show that the compositions of $Ni_xCo_{1-x}(OH)_2$ has a great influence

on overpotentials by comparing multilayer $Co(OH)_2$, $Ni_{0.55}Co_{0.45}(OH)_2$, and $Ni(OH)_2$ for OER. Multilayer $Ni(OH)_2$ exhibits the lowest overpotential of 324 mV at the current density of 5 mA/cm^2. Moreover, the overpotential could be greatly lowered by using single-layer $Ni_xCo_{1-x}(OH)_2$. Single-layer $Ni(OH)_2$ nanosheet manifests 71 mV overpotential decrease (5 mA/cm^2) and a factor of 14 turnover frequency increase as compared to multilayer $Co(OH)_2$ for OER. As for ORR, multilayer $Co(OH)_2$ shows the best activity among multilayer $Ni_xCo_{1-x}(OH)_2$. Similar to OER, single-layer $Ni_xCo_{1-x}(OH)_2$ demonstrates enhanced ORR activity over multilayer $Ni_xCo_{1-x}(OH)_2$. Single-layer $Co(OH)_2$ exhibits the best catalytic activity and 3.7 electrons are transferred during oxygen reduction process. The successful identification of the composition and morphology effect of 3d metal hydroxides on electrocatalytic performance provides the foundation for rational design of active sites for high-performance catalyst for both OER and ORR.

KEYWORDS: *single-layer $Ni_xCo_{1-x}(OH)_2$, oxygen evolution reaction, oxygen reduction reaction*
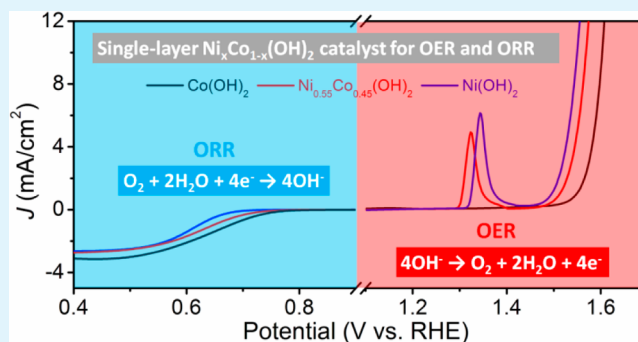
1. INTRODUCTION

The design of cost-effective, highly active catalysts for energy conversion and storage applications is a critical element in the societal pursuit of sustainable energy.[1−4] Among them, catalysts for oxygen evolution reaction (OER) and oxygen reduction reaction (ORR) are at the heart of key renewable-energy technologies including water splitting, lithium−oxygen battery, and fuel cell.[5−10]

OER, in particular, is an important process that enables many energy storage options, such as electricity-driven and direct-solar water splitting. However, the kinetics of OER is sluggish, even after being facilitated by high-activity, precious-metal catalysts. In water-alkali environment, the anodic reaction is a complex process, in which the hydroxyl ions generated at the cathode are consumed at the anode to produce oxygen and water molecules ($4OH^- \leftrightarrow O_2 + 2H_2O + 4e^-$). This process requires a considerable overpotential. Thus, an important issue for OER is to discover and develop catalysts that can reduce the overpotential for OER.[11−13] On the other hand, ORR, the reverse reaction of OER, plays an important role in fuel cell and lithium−air battery. The ORR is a challenging reaction to catalyst in consideration that the catalyst must be stable under the extremely corrosive condition at the cathode, yet chemically active enough to be able to activate oxygen and noble enough to be able to release oxygen from the surface in the form of water. The oxygen activation involves a proton and electron transfer to form adsorbed −OOH before the O−O bond is broken. This requires the catalyst could stabilize −OOH moderately. After

dissociation, adsorbed O and OH are formed on the surface of the catalyst. At this time, a weak binding force between the catalyst and adsorbed O and OH is necessary in order to desorb water quickly.[14−16]

Over the years, a great many materials have been tested for OER and ORR, including various combinations of noble-metal,[17−20] noble-metal alloy,[21−24] 3d-metal (hydro)-oxides,[25−32] phosphates,[33,34] perovskites,[35,36] metal carbides,[37] and advanced carbon materials.[38−42] Among them, noble-metal-based catalysts, RuO_2/IrO_2 for OER,[43] and $Pt_3Ni(111)$ for ORR,[22] present the best activity and stability of all materials. However, the high cost of noble-metal-based catalysts limits their wide application. From a practical point of view, the catalyst should be based on Earth-abundant materials. In consideration of the high-cost of noble metals and low-efficiency of carbon materials, 3d-metal-based catalysts are probably a good option. Among various 3d-metal-based catalysts, cobalt (Co) and nickel (Ni) in the oxide state recently demonstrate their great potential for OER and ORR, which inspires abroad interest from both theoretical and experimental study. Nørskov and Bell calculated the relative stability of Co/Ni in the oxide state and activity trends on this surface via density functional theory (DFT) using the Hubbard-U correction.[44] Dai et al. reported the high active and durable NiFe layered double hydroxide/carbon nanotube hybrid catalyst for OER.[45] These results demonstrated that 3d metal in the oxide state is a promising catalyst for OER and ORR. In addition, Co and Ni, as the members of the group of 3d metals, are prone to hybridize with other elements to form a hybrid catalyst with unprecedented properties, according to a recent report.[46]

Motivated by the previous reports, we report, herein, the investigation of $Ni_xCo_{1-x}(OH)_2$, which was prepared via a wet chemistry method, as a bifunctional electrocatalyst for both OER and ORR. The effect of its compositions (x = 1, 0.55, 0) and morphologies (including both multilayer and single-layer $Ni_xCo_{1-x}(OH)_2$) on catalytic activity is studied systematically in order to optimize the oxygen-electrochemical performance of 3d-M (M = Ni and Co) metal hydroxides. As for OER, the compositions of $Ni_xCo_{1-x}(OH)_2$ has a great influence on overpotentials by comparing multilayer (ML) $Co(OH)_2$, $Ni_{0.55}Co_{0.45}(OH)_2$, and $Ni(OH)_2$. ML $Ni(OH)_2$ exhibits the lowest overpotential of 324 mV at the current density of 5 mA/cm^2. Moreover, the overpotential could be greatly lowered by using single-layer (SL) $Ni_xCo_{1-x}(OH)_2$. We found that SL $Ni(OH)_2$ nanosheets manifests an overpotential decrease of 71 mV (at 5 mA/cm^2) and a factor-of-14 increase in turnover frequency, compared to that for ML $Co(OH)_2$. As for ORR, SL $Co(OH)_2$ exhibits the best catalytic activity and 3.7 electrons are transferred during oxygen reduction process, indicating the low yield of H_2O_2. Our results reveal the trends of oxygen electrochemical activity of wet-chemical-processed $Ni_xCo_{1-x}(OH)_2$ through rational designing materials structure and would provide theoretical guidance for the preparation of next-generation 3d-metal-hydroxide-based heterocatalysts for OER and ORR.

2. MATERIALS AND METHODS

2.1. Materials. Cobalt nitrate hexahydrate ($Co(NO_3)_2 \cdot 6H_2O$) (99.999% trace metal basis), nickel nitrate hexahydrate ($Ni(NO_3)_2 \cdot 6H_2O$) (99.999% trace metal basis), hexamethylenetetramine (HMT) (ACS reagent, ≥99.0%), sodium dodecyl sulfate (SDS) (ACS reagent, ≥99.0%), formamide (ACS reagent, ≥99.5%), potassium hydroxide

(KOH) solution (1 M) were purchased from Sigma−Aldrich. Water was purified immediately before use in a Millipore Direct-Q system.

2.2. Sample Preparation. For the preparation of ML $Co(OH)_2$ or $Ni(OH)_2$, $Co(NO_3)_2 \cdot 6H_2O$ or $Ni(NO_3)_2 \cdot 6H_2O$, SDS, and HMT were dissolved in 50 mL of deionized water to give the final concentrations of 5, 20, and 15 mM in a Teflon beaker filling with nitrogen gas, respectively, and the solution was then heated to 120 °C for 12 h. For the preparation of ML $Ni_{0.55}Co_{0.45}(OH)_2$, the same process as the above was used, where both the concentrations of $Co(NO_3)_2 \cdot 6H_2O$ and $Ni(NO_3)_2 \cdot 6H_2O$ are 2.5 mM. After the reaction, the product was filtered and washed with deionized water and anhydrous ethanol for several times, and finally air-dried at room temperature. For the preparation of SL $Ni_xCo_{1-x}(OH)_2$, 0.2 g as-prepared ML $Ni_xCo_{1-x}(OH)_2$ was mixed with 200 mL of formamide and stirred under nitrogen protection for 72 h. To purify exfoliated product, the resulting solution was centrifuged at 8000 rpm for 10 min to remove nonexfoliated parts.

2.3. Materials Characterization. Scanning electron microscopy (SEM) analysis was performed on a Quanta 400 FEG field-emission scanning electron microscope. Transmission electron microscopy (TEM) analysis was performed on a Tecnai G2 F20 S-Twin field-emission transmission electron microscope. X-ray diffraction (XRD) was collected on a Bruke D8. Electrochemical measurements were performed by an Autolab PGSTAT302N.

2.4. Electrochemical Characterization. For the preparation of ML $Ni_xCo_{1-x}(OH)_2$ catalyst inks, 0.8 mg of ML $Ni_xCo_{1-x}(OH)_2$, 3.2 mg of carbon (Vulcan XC-72), and 20 μL of 5 wt % Nafion solution were dispersed in 2 mL of a water/ethanol (1:1 (v/v)) mixed solvent by at least 30 min of sonication to form a homogeneous ink. Then, 3 μL of catalyst ink (containing 1.2 μg of catalyst) was loaded onto a glassy carbon electrode that had a diameter of 3 mm. For the preparation of SL $Ni_xCo_{1-x}(OH)_2$ catalyst inks, 1 mL of SL $Ni_xCo_{1-x}(OH)_2$ dispersion containing 0.4 mg SL $Ni_xCo_{1-x}(OH)_2$ was mixed with 1.6 mg of carbon (Vulcan XC-72) and 10 μL of 5 wt % Nafion solution. After sonication for at least 30 min, 3 μL of catalyst ink (containing 1.2 μg of catalyst) was loaded onto a glassy carbon electrode that had a diameter of 3 mm. Inductively coupled plasma emission spectrometry−atomic emission spectrometry (ICP-AES) was used to quantify the mass of $Ni_xCo_{1-x}(OH)_2$ in each catalyst ink.

All OER and ORR measurements were conducted in an electrochemical cell using a Ag/AgCl electrode filled with 3 M KCl as the reference electrode, a platinum rod as the counter electrode, and the sample-modified glassy carbon rotating disk electrode (RDE) as the working electrode. Electrolyte was saturated with oxygen by bubbling O_2 prior to the start of each experiment. A flow of O_2 was maintained over the electrolyte during testing in order to ensure its continued O_2 saturation.

For OER measurement (electrolyte is 1 M KOH), linear sweep voltammetry (LSV) was carried out at 5 mV/s with the working electrode continuously rotating at 1600 rpm for the polarization curves. All polarization curves were corrected with iR-compensation. Turnover frequency (TOF) value is calculated from the following equation:

$$TOF = \frac{J \times A}{4 \times F \times m}$$

where J is the current density at overpotential of 0.3 V in A/cm^2, A the area of the electrode, F the Faraday constant, and m the number of moles of the active materials.

For ORR measurement (electrolyte is 0.1 M KOH), the working electrode was scanned cathodically at a rate of 5 mV/s with different rotating speeds, from 400 rpm to 2400 rpm. Koutecky−Levich plots (J^{-1} vs. $\omega^{-1/2}$) were analyzed at various electrode potentials. The slopes of their best linear fit lines were used to calculate the number of transferred electrons (n), based on the Koutecky−Levich equation:

$$\frac{1}{J} = \frac{1}{J_L} + \frac{1}{J_K} = B\omega^{1/2} + \frac{1}{J_K}$$

where

$$B = 0.62nFC_0(D_0)^{2/3}v^{-1/6}$$

$$J_K = nFkC_0$$

J is the measured current density, J_K and J_L are the kinetic- and diffusion-limiting current densities, ω is the angular velocity, n is the number of transferred electrons, F is the Faraday constant, C_0 is the bulk concentration of O_2, D_0 is the diffusion of O_2, v is the kinematic viscosity of the electrolyte, and k is the electron-transfer rate constant. For the Tafel plot, the kinetic current was calculated from the mass-transport correction of RDE by

$$J_K = \frac{J \times J_L}{J_L - J}$$

3. RESULTS AND DISCUSSION

3.1. Preparation and Characterization of ML and SL $Ni_xCo_{1-x}(OH)_2$.
The structure of as-prepared ML $Ni_xCo_{1-x}(OH)_2$—namely, ML $Co(OH)_2$, ML $Ni_{0.55}Co_{0.45}(OH)_2$, and ML $Ni(OH)_2$—were characterized by XRD, as shown in Figure 1. Obviously, they all exhibit the same
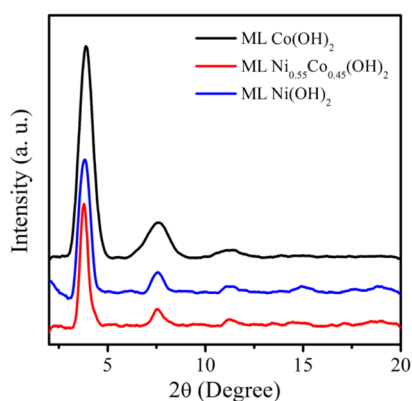

Figure 1. XRD patterns of as-prepared ML $Co(OH)_2$, ML $Ni_{0.55}Co_{0.45}(OH)_2$, and ML $Ni(OH)_2$.

diffraction peaks, which correspond to the d-spacing of 2.4 nm. The appearance of this diffraction peak indicates the multilayered structure of $Ni_xCo_{1-x}(OH)_2$. Previous results have confirmed that the thickness of a single layer of layered double hydroxide nanosheets is ca. 0.8 nm.[47] Therefore, the distance between adjacent layers should be 1.6 nm. The extra distance is ascribed to

the use of dodecyl sulfate as a ligand. Taking the molecular length of dodecyl sulfate (calculated to ca. 1.9 nm) into consideration, it is inferred that the dodecyl sulfate ions are arranged perpendicular to the $Ni_xCo_{1-x}(OH)_2$ nanosheet with a tilt angle of ca. 25°. These results imply that all three $Ni_xCo_{1-x}(OH)_2$ compounds have similar multilayer structures and the interlayer distances are the same. It is worthy to note that, although the molar ratio of Ni and Co is 1:1 in the reaction solution for the preparation of nickel and cobalt mixed hydroxides, the resulting molar ratio of Ni and Co in $Ni_xCo_{1-x}(OH)_2$ product is 55:45, as confirmed by ICP-AES measurement. It is attributed to the different reaction rates of Ni and Co ions and different solubility products of $Ni(OH)_2$ and $Co(OH)_2$ during the formation of $Ni_xCo_{1-x}(OH)_2$, the formula for nickel and cobalt mixed hydroxides is thus recorded as $Ni_{0.55}Co_{0.45}(OH)_2$.[48] In addition, during the preparation of ML $Ni_xCo_{1-x}(OH)_2$, SDS was used as a ligand. A certain amount of dodecyl sulfate anions must exist in the resulting ML $Ni_xCo_{1-x}(OH)_2$ through coordination with part of the nickel or cobalt. Simultaneously, a small amount of crystalliferous water and interlayer water might also exist in the resulting ML $Ni_xCo_{1-x}(OH)_2$. ICP-AES was also used to determine the net weight of ML $Ni_xCo_{1-x}(OH)_2$ precisely. Our results show that the weight percentage of ML $Ni(OH)_2$, $Co(OH)_2$, and $Ni_{0.55}Co_{0.45}(OH)_2$ in the as-prepared products are 68, 68, and 67 wt % with the rests of 32, 32, and 33 wt %, respectively. These results are in good agreement with our previous work.[49,50]

Exfoliation of ML $Ni_xCo_{1-x}(OH)_2$ was conducted in formamide at room temperature. Figure 2 shows the AFM images of exfoliated $Co(OH)_2$ (Figure 2a), $Ni_{0.55}Co_{0.45}(OH)_2$ (Figure 2b), and $Ni(OH)_2$ (Figure 2c), and their corresponding height profiles. All three specimens exhibit a sheetlike structure with the lateral size ranging from tens of nanometers to hundreds of nanometers and heights of ~1 nm, indicating the successful preparation of SL $Co(OH)_2$, $Ni_{0.55}Co_{0.45}(OH)_2$, and $Ni(OH)_2$. Note that the SL $Ni_xCo_{1-x}(OH)_2$ often face restacking, because of their high surface energy. As shown in Figure 2c, the as-prepared SL $Ni(OH)_2$ exhibits little restacking. However, the corresponding height profile clear implies that the height of every SL $Ni(OH)_2$ is ~1 nm.

Similar to other types of 2D materials, SL $Ni_xCo_{1-x}(OH)_2$ are prone to reunite after being dried.[51] To avoid the aggregation of SL $Ni_xCo_{1-x}(OH)_2$ during the preparation of catalyst ink and to improve the conductivity of catalyst also, 80 wt % of Vulcan XC-
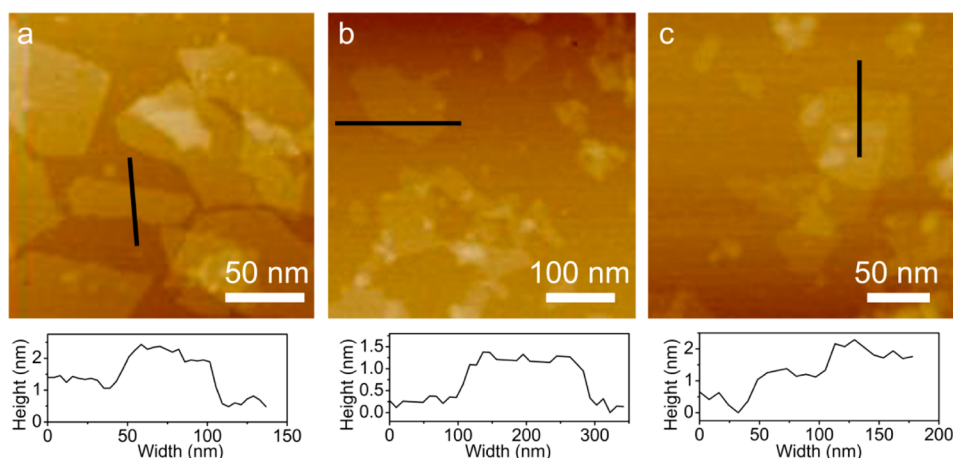

Figure 2. AFM images and corresponding height profiles of (a) SL $Co(OH)_2$, (b) SL $Ni_{0.55}Co_{0.45}(OH)_2$, and (c) SL $Ni(OH)_2$.

72 carbon was added into all three $Ni_xCo_{1-x}(OH)_2$ specimens. Figure 3 shows the TEM images and corresponding energy

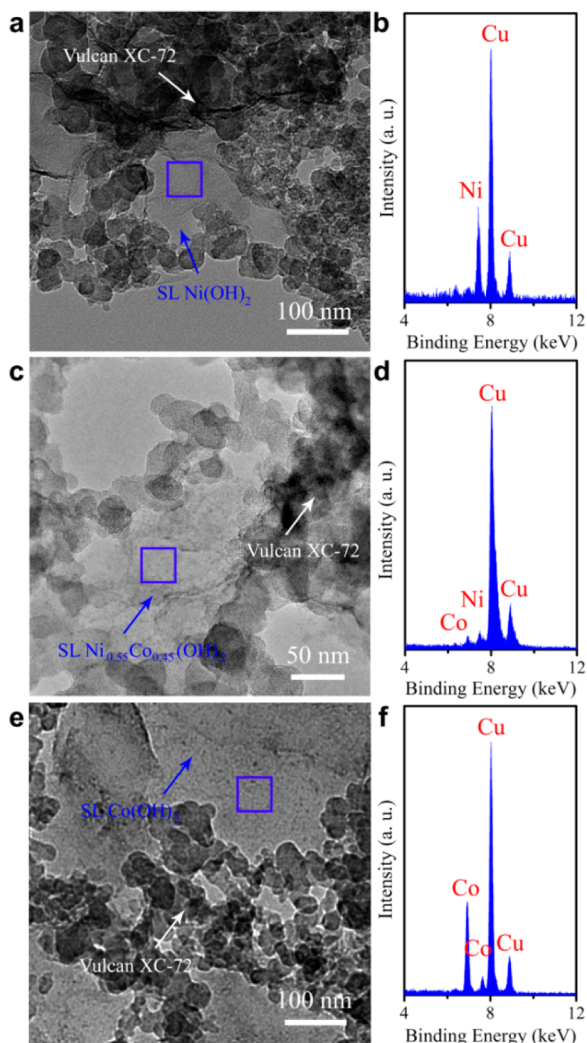**Figure 3.** TEM images and corresponding EDS spectra of (a and b) SL $Co(OH)_2$-based, (c and d) SL $Ni_{0.55}Co_{0.45}(OH)_2$-based, and (e and f) SL $Ni(OH)_2$-based catalysts. EDS spectra were collected in the area as marked by square frames.

dispersive spectrometer (EDS) spectra of the three SL $Ni_xCo_{1-x}(OH)_2$-based catalysts. It can be seen that there is less SL $Ni_xCo_{1-x}(OH)_2$ aggregates in the catalysts, because of the introduction of Vulcan XC-72 carbon.

3.2. OER Activity. For OER measurements, bubbles generated under OER conditions were collected on or near the electrode surface at slower scan rates. As the measurement proceeds, the accumulated bubbles on the electrode surface will cover the surface of the catalyst and cause an additional ohmic resistance, resulting in a decrease in measured current. Herein, all the data for OER are *iR*-compensated.

The OER activity of ML $Ni_xCo_{1-x}(OH)_2$ was first examined. Figure 4a shows the LSV curves of ML $Ni_xCo_{1-x}(OH)_2$. The oxidation peak in the limiting diffusion region can be ascribed to the transformation between $Ni/Co(OH)_2$ and $Ni/CoOOH$ with the process $Ni(OH)_2 + OH^- \leftrightarrow NiOOH + H_2O + e^-$ in an alkaline electrolyte.[52] The oxidation peaks at ~1.33 V and ~1.35 V (vs. RHE) of $Ni(II) \rightarrow Ni(III)$ for ML $Ni_{0.55}Co_{0.45}(OH)_2$ and ML $Ni(OH)_2$, respectively, are observed in Figure 4a. In
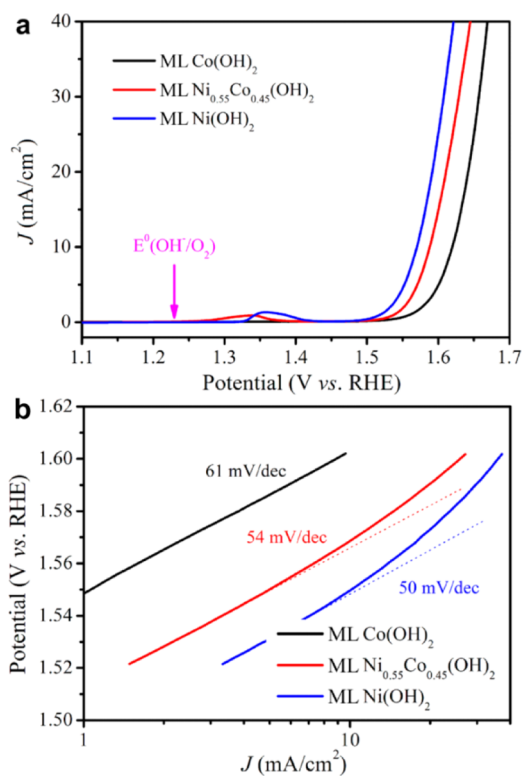
Figure 4. (a) Oxygen evolution currents of ML $Co(OH)_2$, ML $Ni_{0.55}Co_{0.45}(OH)_2$, and ML $Ni(OH)_2$ at a scan rate of 5 mV/s with a rotation of 1600 rpm. (b) Corresponding Tafel plots of OER currents.

addition, there are almost no oxidation peak for ML $Co(OH)_2$. According to the previous reports, the oxidation peak of cobalt in the oxide state is located at ~1.5 V (vs. RHE) in 1 M KOH.[13] Therefore, the oxidation peak of $Co(II) \rightarrow Co(III)$ is overlapped by the polarization in this region. Furthermore, because of the doping of Co atoms in $Ni(OH)_2$, the oxidation peak of $Ni(II) \rightarrow Ni(III)$ for $Ni_{0.55}Co_{0.45}(OH)_2$ shifts slightly more negatively than $Ni(OH)_2$. In LSV curves, apparently, when doping $Co(OH)_2$ with Ni, the onset potential moves to the more-negative region. The OER onset potential for ML $Ni(OH)_2$ is more negative (~1.5 V, relative to RHE) than ML $Co(OH)_2$ and ML $Ni_{0.55}Co_{0.45}(OH)_2$. These results are in agreement with previous reports that the activity of 3d-M hydroxide systems (M = Ni, Co) for monofunctional OER follows the order of Ni > Co, because of the weaker strength of $Ni-OH_{ad}$ (OH_{ad}, defined as the adsorbed OH species) interaction than $Co-OH_{ad}$ interaction.[53] The Tafel slope was collected from Figure 3a where rotating the electrode at 1600 rpm was used to reduce mass transport influence and to increase the potential window. When choosing the region for the Tafel fit, both high potentials at which evolutive oxygen bubbles hinder mass transport and low potentials at which the redox transition of $Ni(II)/Ni(III)$ occurs are avoided. Figure 4b shows that the corresponding Tafel slopes of ML $Co(OH)_2$, ML $Ni_{0.55}Co_{0.45}(OH)_2$, and ML $Ni(OH)_2$ are 61, 54, and 50 mV/dec, respectively, suggesting that ML $Ni(OH)_2$ is a relatively low-polarized catalyst for OER.

The OER activity of SL $Ni_xCo_{1-x}(OH)_2$ was examined in the same way. Figure 5 shows the LSV and Tafel plots for SL $Co(OH)_2$, SL $Ni_{0.55}Co_{0.45}(OH)_2$, and SL $Ni(OH)_2$. The oxidation peaks at ~1.33 and 1.35 V (vs. RHE) of $Ni(II) \rightarrow Ni(III)$ for SL $Ni_{0.55}Co_{0.45}(OH)_2$ and $Ni(OH)_2$, respectively, are observed in Figure 5a. As same as ML $Co(OH)_2$, there are almost
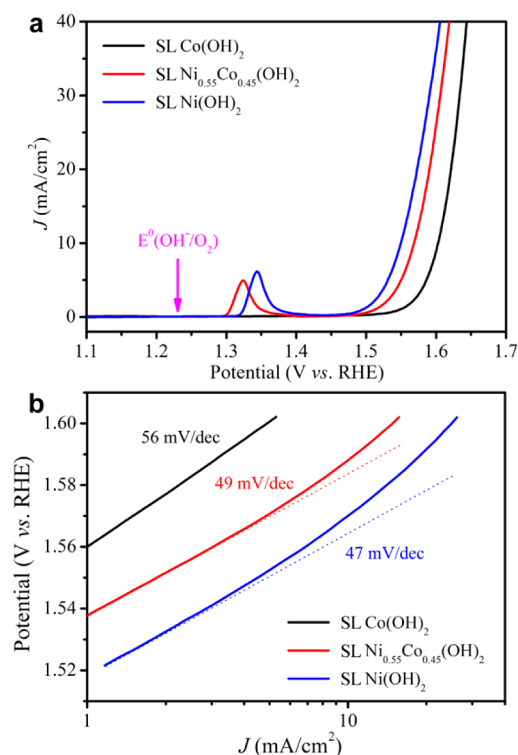
Figure 5. (a) Oxygen evolution currents of SL Co(OH)$_2$, SL Ni$_{0.55}$Co$_{0.45}$(OH)$_2$, and SL Ni(OH)$_2$ at a scan rate of 5 mV/s with a rotation of 1600 rpm. (b) Corresponding Tafel plots of OER currents.

no oxidation peaks for SL Co(OH)$_2$. However, the SL Ni$_{0.55}$Co$_{0.45}$(OH)$_2$ and SL Ni(OH)$_2$ have more sharp oxidation peaks than ML Ni$_{0.55}$Co$_{0.45}$(OH)$_2$ and ML Ni(OH)$_2$ (Figure 4a), indicating the higher electrochemical activity of SL than ML. Furthermore, SL Ni$_x$Co$_{1-x}$(OH)$_2$ demonstrates similar activity trend as ML Ni$_x$Co$_{1-x}$(OH)$_2$. The overpotential decreases as Ni is doped into Co(OH)$_2$. SL Ni(OH)$_2$ shows more positive overpotential than SL Co(OH)$_2$ and SL Ni$_{0.55}$Co$_{0.45}$(OH)$_2$, as shown in Figure 5a. The corresponding Tafel slopes of SL Co(OH)$_2$, SL Ni$_{0.55}$Co$_{0.45}$(OH)$_2$, and SL Ni(OH)$_2$ are 56, 49, and 47 mV/dec, respectively, suggesting that SL Ni(OH)$_2$ is a relatively low-polarized catalyst for OER (see Figure 5b).

To assess our ML Ni$_x$Co$_{1-x}$(OH)$_2$ and the corresponding activity of SL Ni$_x$Co$_{1-x}$(OH)$_2$ for the OER, the specific current density was read at either a constant overpotential of 300 mV or the overpotential at constant specific current densities of 5 and 10 mA cm^{-2} from LSV. The TOF at an overpotential of 300 mV was calculated, and the related results are listed in Table 1.

Table 1. Summary of the OER Activity of ML and SL Ni$_x$Co$_{1-x}$(OH)$_2$

	$J/\eta =$ 300 mV (mA/cm^2)	$\eta/J = 5$ mA/cm^2 (mV)	TOF (s^{-1}) $\eta = 300$ mV	Tafel slope (mV/dec)
ML Co(OH)$_2$	0.329	373	0.0024	61
ML Ni$_{0.55}$Co$_{0.45}$(OH)$_2$	0.658	341	0.0047	54
ML Ni(OH)$_2$	1.675	324	0.0121	50
SL Co(OH)$_2$	0.516	358	0.0037	56
SL Ni$_{0.55}$Co$_{0.45}$(OH)$_2$	2.052	329	0.0148	49
SL Ni(OH)$_2$	4.547	302	0.0327	47

Apparently, the enhancement for OER could be attributed to the more active sites on SL Ni$_x$Co$_{1-x}$(OH)$_2$ than ML Ni$_x$Co$_{1-x}$(OH)$_2$ during the OER operation. As a single-layer 2D materials, all of the atoms in SL Ni$_x$Co$_{1-x}$(OH)$_2$ are exposed to the electrolyte, which is beneficial to maximize the utilization of active materials. As a result, not only are the overpotentials of SL Ni$_x$Co$_{1-x}$(OH)$_2$ at a constant specific current of 5 mA cm^{-2} reduced, but the TOF of SL Ni$_x$Co$_{1-x}$(OH)$_2$ also are improved greatly, compared to that of ML Ni$_x$Co$_{1-x}$(OH)$_2$, where the TOF of SL Ni(OH)$_2$ is ~16 times higher than that of ML Co(OH)$_2$.

To compare the different durability of SL Ni$_x$Co$_{1-x}$(OH)$_2$ and ML Ni$_x$Co$_{1-x}$(OH)$_2$, the chronoamperometric responses (percentage of potential versus operation time) of both ML Ni$_x$Co$_{1-x}$(OH)$_2$ and SL Ni$_x$Co$_{1-x}$(OH)$_2$ were examined (Figure 6). All the data from the measurements are normalized. It shows
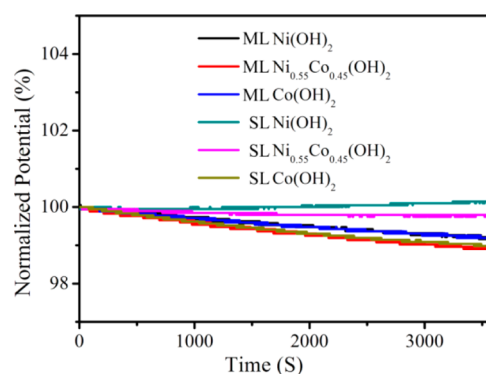

Figure 6. Chronopotentialmetric response (percentage of potential versus operation time) of ML Ni$_x$Co$_{1-x}$(OH)$_2$ and SL Ni$_x$Co$_{1-x}$(OH)$_2$ at 5 mA/cm^2 in O$_2$-saturated 1 M KOH electrolyte.

that SL Ni$_x$Co$_{1-x}$(OH)$_2$ presents a better durability than ML Ni$_x$Co$_{1-x}$(OH)$_2$. Among them, SL Ni(OH)$_2$ displays the best durability, so that there is almost no decay during the entire test.

3.3. ORR Activity. It is generally acknowledged that transition-metal-based catalysts are bifunctional catalysts for both ORR and OER, and sometimes the activity trend in ORR is opposite to OER. Therefore, it is worthy to investigate the ORR activity of ML Ni$_x$Co$_{1-x}$(OH)$_2$ and SL Ni$_x$Co$_{1-x}$(OH)$_2$. For ORR measurements, both ML Ni$_x$Co$_{1-x}$(OH)$_2$- and SL Ni$_x$Co$_{1-x}$(OH)$_2$-based catalysts were loaded onto the glassy carbon electrodes (with the same mass loading) in O$_2$-saturated 0.1 M KOH, respectively. Voltammograms were recorded until the redox peaks and the oxygen reduction currents show negligible change, typically after 5−10 cycles.

CV curves of ML Ni$_x$Co$_{1-x}$(OH)$_2$ are shown in Figure 7a. The ML Co(OH)$_2$ presents the most-positive ORR onset potential (~0.78 V, relative to the RHE) and highest cathodic current among the three specimens. It indicates a better ORR activity of ML Co(OH)$_2$ than those of ML Ni$_{0.55}$Co$_{0.45}$(OH)$_2$ and ML Ni(OH)$_2$. To investigate the kinetics of ML Ni$_x$Co$_{1-x}$(OH)$_2$, the rotating-disk measurements in O$_2$-saturated 0.1 M KOH electrolytes at a scan rate of 5 mV/s with different rotation rates were carried out (see Figures 7b, 7c, and 7d). The corresponding electron transfer number (n) was calculated from the slopes of Koutecky−Levich plots at 0.35, 0.40, 0.45, and 0.50 V (inset of Figures 7b, 7c, and 7d). As a result, the electron transfer numbers of ML Ni(OH)$_2$ and ML Ni$_{0.55}$Co$_{0.45}$(OH)$_2$ are calculated to be 2.1 and 2.5, respectively. In contrast, the ML Co(OH)$_2$ shows the highest electron transfer number, up to 3.1.
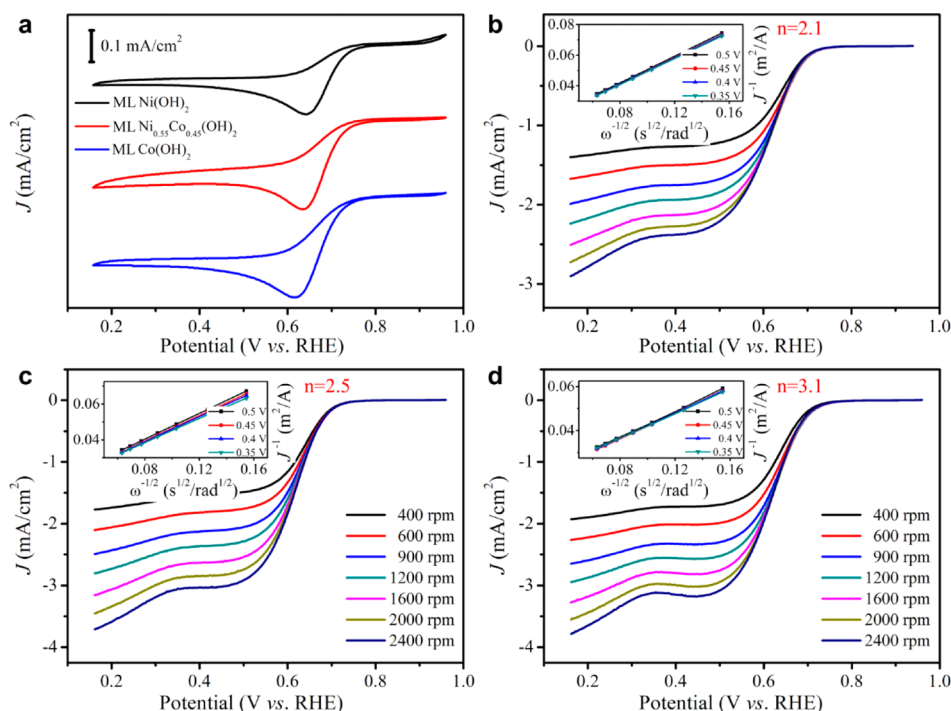
Figure 7. (a) CV curves of ML Ni(OH)$_2$, ML Ni$_{0.55}$Co$_{0.45}$(OH)$_2$, and ML Co(OH)$_2$ in O$_2$-saturated 0.1 M KOH electrolytes at a scan rate of 5 mV/s. Rotating-disk voltammograms of (b) ML Ni(OH)$_2$, (c) ML Ni$_{0.55}$Co$_{0.45}$(OH)$_2$, and (d) ML Co(OH)$_2$ in O$_2$-saturated 0.1 M KOH electrolytes at a scan rate of 5 mV/s at the different rotation rates. The inset in panels b, c, and d show corresponding Koutecky−Levich plots (J^{-1} vs $\omega^{-0.5}$) at different potentials.

It reveals that ML Co(OH)$_2$ is a most effective catalyst for ORR and produces less H$_2$O$_2$ during the ORR process.

Figure 8a shows the comparison of LSV curves of ML Ni$_x$Co$_{1-x}$(OH)$_2$ at a scan rate of 5 mV/s with the rotation of 1600 rpm. The half-wave potentials are 0.611 V vs RHE for ML Ni(OH)$_2$, 0.625 V vs RHE for ML Ni$_{0.55}$Co$_{0.45}$(OH)$_2$, and 0.627 V vs RHE for ML Co(OH)$_2$, respectively. Apparently, ML Co(OH)$_2$ represents the most-positive half-wave potential among ML Ni$_x$Co$_{1-x}$(OH)$_2$. Correspondingly, ML Co(OH)$_2$ also exhibits a much smaller Tafel slope (59 mV/dec) than that of ML Ni$_x$Co$_{1-x}$(OH)$_2$ and ML Ni(OH)$_2$ (Figure 8b), suggesting its excellent ORR activity.

The ORR activity of SL Ni$_x$Co$_{1-x}$(OH)$_2$ was examined in the same way (Figure 9). SL Ni$_x$Co$_{1-x}$(OH)$_2$ displays electrochemical behavior similar to that of ML Ni$_x$Co$_{1-x}$(OH)$_2$. The SL Co(OH)$_2$ NSs still possesses the best performance among SL Ni$_x$Co$_{1-x}$(OH)$_2$. The onset potential of SL Co(OH)$_2$ is obviously positive (∼0.82 V relative to the RHE) and the cathodic current is higher than SL Ni$_{0.55}$Co$_{0.45}$(OH)$_2$ and SL Ni(OH)$_2$ (Figure 9a). When compared with ML Ni$_x$Co$_{1-x}$(OH)$_2$, SL Ni$_x$Co$_{1-x}$(OH)$_2$ presents enhanced activity for ORR, which is similar to the OER activity. We also analyzed the electron transfer number of SL Ni$_x$Co$_{1-x}$(OH)$_2$. It shows that the electron transfer numbers of SL Ni$_x$Co$_{1-x}$(OH)$_2$ are all higher than the corresponding ML Ni$_x$Co$_{1-x}$(OH)$_2$: 2.3 for SL Ni(OH)$_2$, 3.3 for SL Ni$_{0.55}$Co$_{0.45}$(OH)$_2$, and 3.7 for SL Co(OH)$_2$ (see Figures 9b, 9c, and 9d). These results demonstrate that single-layer transition-metal hydroxides nanosheets are advantageous to enhance the activity of ORR. The large electron transfer number of SL Co(OH)$_2$ reveals that the ORR in SL Co(OH)$_2$ is dominated by a four-electron process and oxygen is directly reduced to a hydroxyl ion.
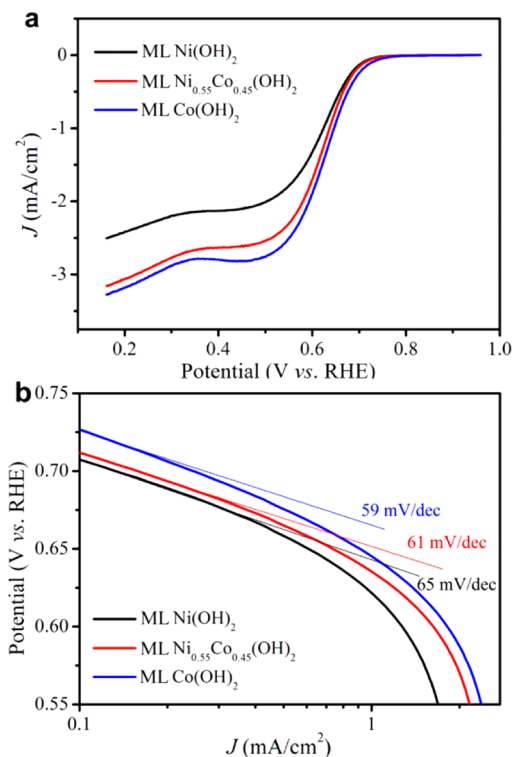

Figure 8. (a) LSV and (b) corresponding Tafel plots of ML Ni(OH)$_2$, ML Ni$_{0.55}$Co$_{0.45}$(OH)$_2$, and ML Co(OH)$_2$, in O$_2$-saturated 0.1 M KOH electrolytes at a scan rate of 5 mV/s with the rotation of 1600 rpm.

Figure 10a shows the LSV curves of SL Ni$_x$Co$_{1-x}$(OH)$_2$ at a scan rate of 5 mV/s with the rotation of 1600 rpm. The half-wave potentials are 0.641 V vs RHE for SL Ni(OH)$_2$, 0.629 V vs RHE
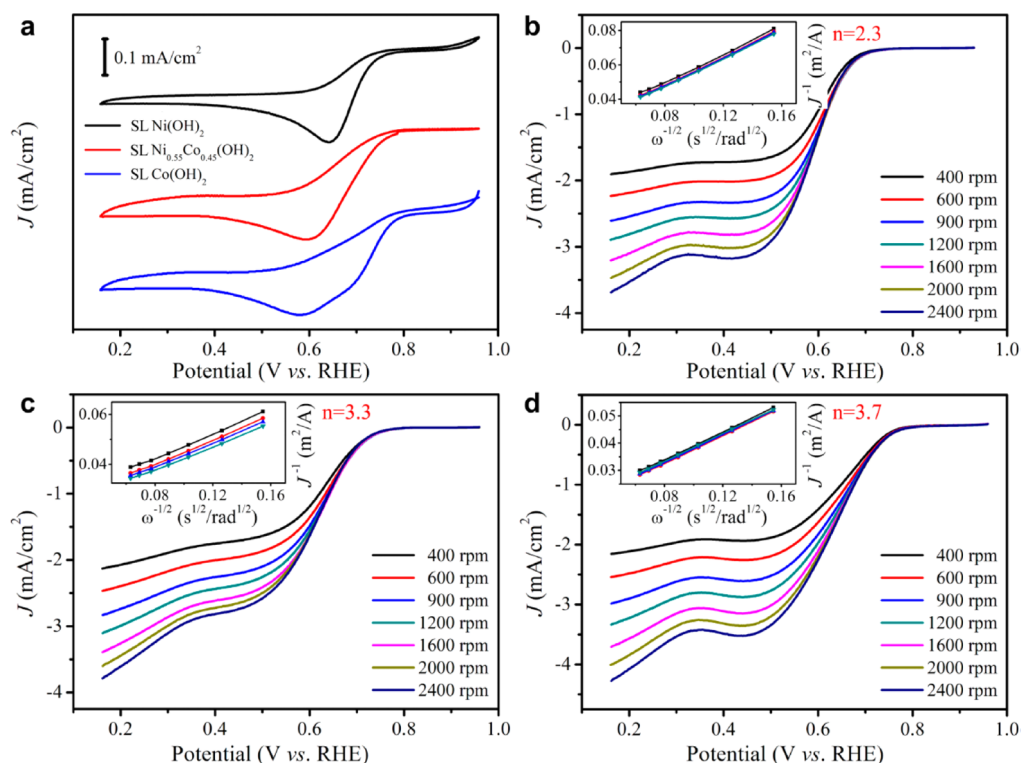
Figure 9. (a) CV curves of SL $Ni(OH)_2$, SL $Ni_{0.55}Co_{0.45}(OH)_2$, and SL $Co(OH)_2$ in O_2-saturated 0.1 M KOH electrolytes at a scan rate of 5 mV/s. Rotating-disk voltammograms of (b) SL $Ni(OH)_2$, (c) SL $Ni_{0.55}Co_{0.45}(OH)_2$, and (d) SL $Co(OH)_2$ in O_2-saturated 0.1 M KOH electrolytes at a scan rate of 5 mV/s at the different rotation rates. The insets in panels b, c, and d show corresponding Koutecky−Levich plots (J^{-1} vs $\omega^{-0.5}$) at different potentials.
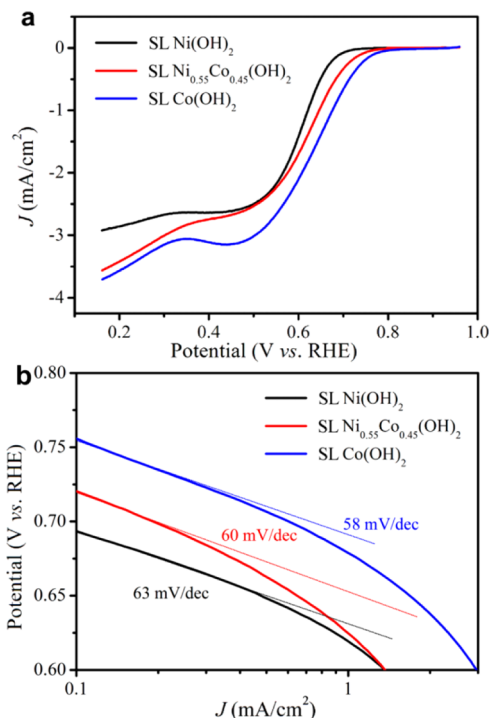

Figure 10. (a) LSV and (b) corresponding Tafel plots of SL $Ni(OH)_2$, SL $Ni_{0.55}Co_{0.45}(OH)_2$, and SL $Co(OH)_2$ in O_2-saturated 0.1 M KOH electrolytes at a scan rate of 5 mV/s with a rotation of 1600 rpm.

for SL $Ni_{0.55}Co_{0.45}(OH)_2$, and 0.614 V vs RHE for SL $Co(OH)_2$, respectively. Tafel plots show that SL $Ni_xCo_{1-x}(OH)_2$ have smaller Tafel slopes of ORR than ML $Ni_xCo_{1-x}(OH)_2$, which are

similar to the results as observed in the Tafel slopes of OER. SL $Co(OH)_2$ exhibits the smallest Tafel slope (58 mV/dec), compared to SL $Ni_xCo_{1-x}(OH)_2$ and $Ni(OH)_2$. The half-wave potential, electron transfer number, and Tafel slope of both ML $Ni_xCo_{1-x}(OH)_2$ and SL $Ni_xCo_{1-x}(OH)_2$ are listed in Table 2. It is clear that reducing the dimension of $Ni_xCo_{1-x}(OH)_2$ could effectively improve the ORR activity.

Table 2. Summary of the ORR Activity of ML and SL $Ni_xCo_{1-x}(OH)_2$ (Half Wave Potential Was Collected at 1600 rpm)

	electron transfer number	half wave potential (V)	Tafel slope (mV/dec)
ML $Ni(OH)_2$	2.1	0.611	65
ML $Ni_{0.55}Co_{0.45}(OH)_2$	2.5	0.625	61
ML $Co(OH)_2$	3.1	0.627	59
SL $Ni(OH)_2$	2.3	0.614	63
SL $Ni_{0.55}Co_{0.45}(OH)_2$	3.3	0.629	60
SL $Co(OH)_2$	3.7	0.641	58

To further compare the different durability of SL $Ni_xCo_{1-x}(OH)_2$ and ML $Ni_xCo_{1-x}(OH)_2$, chronoamperometric response (percentage of potential versus operation time) of both ML $Ni_xCo_{1-x}(OH)_2$ and SL $Ni_xCo_{1-x}(OH)_2$ were examined (Figure 11). All the data are normalized by the data of SL $Co(OH)_2$. Apparently, SL $Ni_xCo_{1-x}(OH)_2$ generally presents a better durability with the minimum decline during the entire test. Among them, SL $Co(OH)_2$ demonstrates the best durability, so that ∼70% activity after 10 000 s is achieved, indicating a good
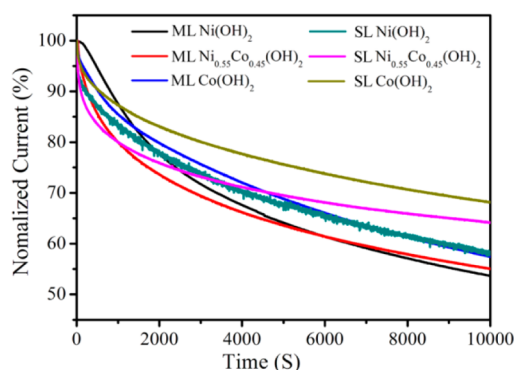
Figure 11. Chronoamperometric response (percentage of potential versus operation time) of ML and SL $Ni_xCo_{1-x}(OH)_2$ kept at 0.5 V versus RHE in O_2-saturated 0.1 M KOH electrolyte.

lifetime for ORR. In contrast, ML $Ni(OH)_2$ exhibits the worst durability, so that only 53% activity after 10 000 s is maintained.

4. CONCLUSION

In summary, we prepared a series of $Ni_xCo_{1-x}(OH)_2$-based catalysts for OER or ORR and systematically investigated the influence of the composition and morphology of $Ni_xCo_{1-x}(OH)_2$ on electrochemical activity. To our knowledge, this is the first time that single-layer $Ni_xCo_{1-x}(OH)_2$ was employed as bifunctional catalyst for ORR and OER and compared with as-prepared multilayered $Ni_xCo_{1-x}(OH)_2$. Our result demonstrated that single-layer $Ni_xCo_{1-x}(OH)_2$ exhibits the superior oxygen electrochemical activity to multilayered $Ni_xCo_{1-x}(OH)_2$, because of the greater number of active sites exposed on the surfaces or edges in single-layer nanosheets. It could be concluded that the OER and ORR activity of transition-metal hydroxide could be indeed improved by tuning the morphology and composition. The performance of our materials could be further improved by forming the composites with a high-electron-transfer matrix.

ASSOCIATED CONTENT

Ⓢ Supporting Information
Summary of literature Tafel slopes of various Ni/Co-based OER catalysts and corresponding reference. This material is available free of charge via the Internet at http://pubs.acs.org.

AUTHOR INFORMATION

Corresponding Author
*E-mail: jjin2009@sinano.ac.cn.

Author Contributions
¶These authors contributed equally.

Notes
The authors declare no competing financial interest.

ACKNOWLEDGMENTS

REFERENCES

(1) Greeley, J.; Jaramillo, T. F.; Bonde, J.; Chorkendorff, I.; Nørskov, J. K. Computational High-Throughput Screening of Electrocatalytic Materials for Hydrogen Evolution. *Nat. Mater.* **2006**, *5*, 909−913.

(2) Chu, S.; Majumdar, A. Opportunities and Challenges for A Sustainable Energy Future. *Nature* **2012**, *488*, 294−303.

(3) Greeley, J.; Markovic, N. M. The Road From Animal Electricity to Green Energy: Combining Experiment and Theory in Electrocatalysis. *Energy Environ. Sci.* **2012**, *5*, 9246−9256.

(4) Koper, M. T. M. Hydrogen Electrocatalysis: A Basic Solution. *Nat. Chem.* **2013**, *5*, 255−256.

(5) Gray, H. B. Powering the Planet with Solar Fuel. *Nat. Chem.* **2009**, *1*, 7.

(6) Kudo, A.; Miseki, Y. Heterogeneous Photocatalyst Materials for Water Splitting. *Chem. Soc. Rev.* **2009**, *38*, 253−278.

(7) Walter, M. G.; Warren, E. L.; McKone, J. R.; Boettcher, S. W.; Mi, Q.; Santori, E. A.; Lewis, N. S. Solar Water Splitting Cells. *Chem. Rev.* **2010**, *110*, 6446−6473.

(8) Kudo, A. Z-Scheme Photocatalyst Systems for Water Splitting Under Visible Light Irradiation. *MRS Bull.* **2011**, *36*, 32−38.

(9) Cheng, F. Y.; Chen, J. Metal-Air Batteries: From Oxygen Reduction Electrochemistry to Cathode Catalysts. *Chem. Soc. Rev.* **2012**, *41*, 2172−2192.

(10) Wang, H.; Dai, H. Strongly Coupled Inorganic-Nano-Carbon Hybrid Materials for Energy Storage. *Chem. Soc. Rev.* **2013**, *42*, 3088−3113.

(11) Jiao, F.; Frei, H. Nanostructured Cobalt Oxide Clusters in Mesoporous Silica as Efficient Oxygen-Evolving Catalysts. *Angew. Chem., Int. Ed.* **2009**, *48*, 1841−1844.

(12) Esswein, A. J.; McMurdo, M. J.; Ross, P. N.; Bell, A. T.; Tilley, T. D. Size-Dependent Activity of Co_3O_4 Nanoparticle Anodes for Alkaline Water Electrolysis. *J. Phys. Chem. C* **2009**, *113*, 15068−15072.

(13) Yeo, B. S.; Bell, A. T. Theoretical Investigation of the Activity of Cobalt Oxides for the Electrochemical Oxidation of Water. *J. Am. Chem. Soc.* **2011**, *133*, 5587−5593.

(14) Yeager, E. Electrocatalysts for O_2 Reduction. *Electrochim. Acta* **1984**, *29*, 1527−1537.

(15) Shao-Horn, Y.; Sheng, W. C.; Chen, S.; Ferreira, P. J.; Holby, E. F.; Morgan, D. Instability of Supported Platinum Nanoparticles in Low-Temperature Fuel Cells. *Top. Catal.* **2007**, *46*, 285−305.

(16) Gewirth, A. A.; Thorum, M. S. Electroreduction of Dioxygen for Fuel-Cell Applications: Materials and Challenges. *Inorg. Chem.* **2010**, *49*, 3557−3566.

(17) Adzić, R. R.; Marković, N. M.; Vešović, V. B. Structural Effects in Electrocatalysis: Oxygen Reduction on the Au(100) Single Crystal Electrode. *J. Electroanal. Chem.* **1984**, *165*, 105−120.

(18) Kinoshita, K. J. Particle Size Effects for Oxygen Reduction on Highly Dispersed Platinum in Acid Electrolytes. *J. Electrochem. Soc.* **1990**, *137*, 845−848.

(19) Li, X.; Gewirth, A. A. Oxygen Electroreduction through a Superoxide Intermediate on Bi-Modified Au Surfaces. *J. Am. Chem. Soc.* **2005**, *127*, 5252−5260.

(20) Mayrhofer, K. J. J.; Strmcnik, D.; Blizanac, B. B.; Stamenkovic, V.; Arenz, M.; Markovic, N. M. Measurement of Oxygen Reduction Activities via the Rotating Disc Electrode Method: From Pt Model Surfaces to Carbon-Supported High Surface Area Catalysts. *Electrochim. Acta* **2008**, *53*, 3181−3188.

(21) Stamenkovic, V.; Mun, B. S.; Mayrhofer, K. J. J.; Ross, P. N.; Markovic, N. M.; Rossmeisl, J.; Greeley, J.; Norskov, J. K. Changing the Activity of Electrocatalysts for Oxygen Reduction by Tuning the Surface Electronic Structure. *Angew. Chem., Int. Ed.* **2006**, *45*, 2897−2901.

(22) Stamenkovic, V. R.; Fowler, B.; Mun, B. S.; Wang, G. F.; Ross, P. N.; Lucas, C. A.; Markovic, N. M. Improved Oxygen Reduction Activity on $Pt_3Ni(111)$ via Increased Surface Site Availability. *Science* **2007**, *315*, 493−497.

(23) Wang, D.; Xin, H. L.; Hovden, R.; Wang, H.; Yu, Y.; Muller, D. A.; Disalvo, F. J.; Abruňa, H. D. Structurally Ordered Intermetallic Platinum-Cobalt Core-Shell Nanoparticles with Enhanced Activity

and Stability as Oxygen Reduction Electrocatalysts. *Nat. Mater.* **2013**, *12*, 81−87.

(24) Cui, C.; Gan, L.; Heggen, M.; Rudi, S.; Strasser, P. Compositional Segregation in Shaped Pt Alloy Nanoparticles and Their Structural Behaviour during Electrocatalysis. *Nat. Mater.* **2013**, *12*, 765−771.

(25) Bashyam, R.; Zelenay, P. A Class of Non-Precious Metal Composite Catalysts for Fuel Cells. *Nature* **2006**, *443*, 63−66.

(26) Wang, C.; Daimon, H.; Sun, S. Dumbbell-like Pt−Fe_3O_4 Nanoparticles and Their Enhanced Catalysis for Oxygen Reduction Reaction. *Nano Lett.* **2009**, *91*, 1493−1496.

(27) Liang, Y.; Wang, H.; Diao, P.; Chang, W.; Hong, G.; Li, Y.; Gong, M.; Xie, L.; Zhou, J.; Wang, J.; Regier, T. Z.; Wei, F.; Dai, H. Oxygen Reduction Electrocatalyst Based on Strongly Coupled Cobalt Oxide Nanocrystals and Carbon Nanotubes. *J. Am. Chem. Soc.* **2012**, *134*, 15849−15857.

(28) Wu, Z.; Yang, S.; sun, Y.; Parvez, K.; Feng, X.; Müllen, K. Three-Dimensional Graphene-Based Macro-and Mesoporous Frameworks for High-Performance Electrochemical Capacitive Energy Storage. *J. Am. Chem. Soc.* **2012**, *134*, 9082−9085.

(29) Warren, S. C.; Voïtchovsky, K.; Dotan, H.; Leroy, C. M.; Cornuz, M.; Stellacci, F.; Hébert, C.; Rothschild, A.; Grätzel, M. Identifying Champion Nanostructures for Solar Water-Splitting. *Nat. Mater.* **2013**, *12*, 842−849.

(30) Gao, M.; Xu, Y.; Jiang, J.; Zheng, Y.; Yu, S. Water Oxidation Electrocatalyzed by an Efficient $Mn_3O_4/CoSe_2$ Nanocomposite. *J. Am. Chem. Soc.* **2012**, *134*, 2930−2933.

(31) Louie, M. W.; Bell, A. T. An Investigation of Thin-Film Ni-Fe Oxide Catalysts for the Electrochemical Evolution of Oxygen. *J. Am. Chem. Soc.* **2013**, *135*, 12329−12337.

(32) Blakemore, J. D.; Gray, H. B.; Winkler, J. R.; Müller, A. M. Co_3O_4 Nanoparticle Water-Oxidation Catalysts Made by Pulsed-Laser Ablation in Liquids. *ACS Catal.* **2013**, *3*, 2497−2500.

(33) Kanan, M. W.; Nocera, D. G. In Situ Formation of an Oxygen-Evolving Catalyst in Neutral Water Containing Phosphate and Co^{2+}. *Science* **2008**, *321*, 1072−1075.

(34) Kanan, M. W.; Yano, J.; Surendranath, Y.; Dincǎ, M.; Yachandra, V. K.; Nocera, D. G. Mechanistic Studies of the Oxygen Evolution Reaction by a Cobalt-Phosphate Catalyst at Neutral pH. *J. Am. Chem. Soc.* **2010**, *132*, 13692−13701.

(35) Suntivich, J.; May, K. J.; Gasteiger, H. A.; Goodenough, J. B.; Shao-Horn, Y. A Perovskite Oxide Optimized for Oxygen Evolution Catalysis from Molecular Orbital Principles. *Science* **2011**, *334*, 1383−1385.

(36) May, K. J.; Carlton, C. E.; Stoerzinger, K. A.; Risch, M.; Suntivich, J.; Lee, Y.; Grimaud, A.; Shao-Horn, Y. Influence of Oxygen Evolution During Water Oxidation on the Surface of Perovskite Oxide Catalysts. *J. Phys. Chem. Lett.* **2012**, *3*, 3264−6270.

(37) Liu, Y.; Kelly, T. G.; Chen, J. G.; Mustain, W. E. Metal Carbides as Alternative Electrocatalyst Supports. *ACS Catal.* **2013**, *3*, 1184−1194.

(38) Liang, Y.; Li, Y.; Wang, H.; Zhou, J.; Wang, J.; Regier, T.; Dai, H. Co_3O_4 Nanocrystals on Graphene as a Synergistic Catalyst for Oxygen Reduction Reaction. *Nat. Mater.* **2011**, *10*, 780−786.

(39) Li, Y.; Zhou, W.; Wang, H.; Xie, L.; Liang, Y.; Wei, F.; Idrobo, J.; Pennycook, S. J.; Dai, H. An Oxygen Reduction Electrocatalyst Based on Carbon Nanotube-Graphene Complexes. *Nat. Nanotechnol.* **2012**, *7*, 394−400.

(40) Liang, J.; Jiao, Y.; Jaroniec, M.; Qiao, S. Z. Sulfur and Nitrogen Dual-Doped Mesoporous Graphene Electrocatalyst for Oxygen Reduction with Synergistically Enhanced Performance. *Angew. Chem., Int. Ed.* **2012**, *21*, 11496−11500.

(41) Chung, H. T.; Won, J. H.; Zelenay, P. Active and Stable Carbon Nanotube/Nanoparticle Composite Electrocatalyst for Oxygen Reduction. *Nat. Commun.* **2013**, *4*, 1922.

(42) Zhao, Y.; Nakamura, R.; Kamiya, K.; Nakanishi, S.; Hashimoto, K. Nitrogen-Doped Carbon Nanomaterials as Non-Metal Electrocatalysts for Water Oxidation. *Nat. Commun.* **2013**, *4*, 2390.

(43) Reier, T.; Oezaslan, M.; Strasser, P. Electrocatalytic Oxygen Evolution Reaction (OER) on Ru, Ir, and Pt Catalysts: A Comparative Study of Nanoparticles and Bulk Materials. *ACS Catal.* **2012**, *2*, 1765−1772.

(44) Bajdich, M.; García-Mota, M.; Vojvodic, A.; Nørskov, J. K.; Bell, A. T. Theoretical Investigation of the Activity of Cobalt Oxides for the Electrochemical Oxidation of Water. *J. Am. Chem. Soc.* **2013**, *135*, 13521−13520.

(45) Gong, M.; Li, Y.; Wang, H.; Liang, Y.; Wu, J. Z.; Zhou, J.; Wang, J.; Regier, T.; Wei, F.; Dai, H. An Advanced Ni-Fe Layered Double Hydroxide Electrocatalyst for Water Oxidation. *J. Am. Chem. Soc.* **2013**, *135*, 8452−8455.

(46) Subbaraman, R.; Tripkovic, D.; Strmcnik, D.; Chang, K.; Uchimura, M.; Paulikas, A. P.; Stamenkovic, V.; Markovic, N. M. Enhancing Hydrogen Evolution Activity in Water Splitting by Tailoring Li^+-Ni$(OH)_2$-Pt Interfaces. *Science* **2011**, *334*, 1256−1260.

(47) Wang, L.; Dong, Z.; Wang, Z.; Zhang, F.; Jin, J. Layered α-Co$(OH)_2$ Nanocones as Electrode Materials for Pseudocapacitors: Understanding the Effect of Interlayer Space on Electrochemical Activity. *Adv. Funct. Mater.* **2013**, *23*, 2758−2764.

(48) Boclair, J. W.; Braterman, P. S. Layered Double Hydroxide Stability. 1. Relative Stabilities of Layered Double Hydroxides and Their Simple Counterparts. *Chem. Mater.* **1999**, *11*, 298−302.

(49) Wang, L.; Wang, D.; Dong, X.; Zhang, Z.; Pei, X.; Chen, X.; Chen, B.; Jin, J. Layered Assembly of Graphene Oxide and Co-Al Layered Double Hydroxide Nanosheets as Electrode Materials for Super-capacitors. *Chem. Commun.* **2011**, *47*, 3556−3558.

(50) Wang, L.; Lin, C.; Zhang, F.; Jin, J. Phase Transformation Guided Single-Layer β-Co$(OH)_2$ Nanosheets for Pseudocapacitive Electrodes. *ACS Nano* **2014**, *8*, 3724−3734.

(51) Liu, Z.; Ma, R.; Osada, M.; Iyi, N.; Ebina, Y.; Takada, K.; Sasaki, T. Synthesis, Anion Exchange, and Delamination of Co-Al Layered Double Hydroxide: Assembly of the Exfoliated Nanosheet/Polyanion Composite Films and Magneto-Optical Studies. *J. Am. Chem. Soc.* **2006**, *128*, 4872−4880.

(52) Trotochaud, L.; Ranney, J. K.; Williams, K. N.; Boettcher, S. W. Solution-Cast Metal Oxide Thin Film Electrocatalysts for Oxygen Evolution. *J. Am. Chem. Soc.* **2012**, *134*, 17253−17261.

(53) Subbaraman, R.; Tripkovic, D.; Chang, K.; Strmcnik, D.; Paulikas, A. P.; Hirunsit, P.; Chan, M.; Greeley, J.; Stamenkovic, V.; Markovic, N. M. Trends in Activity for the Water Electrolyser Reactions on 3d M(Ni, Co, Fe, Mn) Hydr(oxy)oxide Catalysts. *Nat. Mater.* **2012**, *11*, 550−557.